Green Visible light catalysis for dye effluent Degradation with special reference Alizarin red and Antibacterial activity using $SrFe_{12}O_{19}/TiO_2/SiO_2/GO$ Nanocomposite

Suneetha M[*1], Hima Bindu G[*1], Ramya Kumari Ch[1], Jyothi Priya K[1], Swapna D[1,2], Jayashree R[1], Paul Douglas S [*1]

[1]Department of Engineering Chemistry, Andhra University College of Engineering, Andhra University (A), Visakhapatnam- 530003, Andhra Pradesh, INDIA
[2]Dadi Institute of Engineering and Technology, Anakapalli – 531002

maheshhanisony@gmail.com; pauldouglas12@gmail.com; himabinduauce@gmail.com

Abstract. For the photocatalytic degradation of dye, ternary metal oxides ($SrFe_{12}O_{19}/TiO_2/SiO_2$) and their nanocomposites with graphene oxide were produced using the Sol-gel and Hummers' process, respectively. UV–Vis diffuse reflection spectroscopy (DRS) revealed that the samples a low band gap of 2.29 eV. The reduced band gap of $SrFe_{12}O_{19}/TiO_2/SiO_2/GO$ resulted in significantly enhanced photocatalytic activity compared to the bare photocatalysts. The calcined samples of $SrFe_{12}O_{19}/TiO_2/SiO_2/GO$ showed optimal photocatalytic performance, achieving 100% degradation of Alizarin red dye under visible light irradiation within 60 minutes at pH-6 (dye concentration 10ppm). Scanning electron microscopy (SEM) and X-ray diffraction (XRD) were in used to assess the phase purity, structural properties and surface morphology of the prepared nanomaterials and their nanocomposites. Fourier-transform infrared (FTIR) spectroscopy was used to identify the functional groups in the manufactured metal oxides, confirming the presence of M − O (metal-oxygen) bonds. Vibrating sample magnetometry (VSM) was familiar analyze the magnetic properties of the composite particles. The outcomes demonstrated that the $SrFe_{12}O_{19}/TiO_2/SiO_2/GO$ composite particles consisted of spherical nanoparticles approximately 30 nm in diameter**.** The antibacterial activity of the nanocomposites was tested against Gram-negative *Pseudomonus aeruginosa* (ATCC-15692) and Gram-positive *Micrococcus luteus* (ATCC 9341)bacteria. Moreover, $SrFe_{12}O_{19}$ nanoparticles possess excellent magnetic properties, which are largely retained in the TSG composite and can be easily separated from suspension by applying a magnetic field. These magnetic composite nanoparticles demonstrated substantial photocatalytic efficiency, making them promising for water remediation.

R. K. Ramachandra et al. (eds.), *Proceedings of the International Conference on Bio-Based Environment for Sustainable Territory (IC-BEST 2024)*, Advances in Biological Sciences Research 44,
https://doi.org/10.2991/978-94-6463-648-2_16

Keywords: SrFe $_{12}O_{19}$ /TiO $_2$ /SiO $_2$ /GO, Sol-gel Method, Hummers Method, Photocatalytic Activity, Nanocomposite, Alizarin red dye, Antibacterial activity

1. Introduction: Wastewaters from textile and dyeing industries contain high levels of various non-biodegradable dyes, which lead to significant environmental issues [1]. This problem is worsened by population growth and rapid industrial expansion, which increase the release of carcinogenic, toxic, or mutagenic compounds, posing risks to all living organisms [2]. A water-soluble anthraquinone dye Alizarin Red S ($C_{14}H_7NaO_7S \cdot H_2O$) (AR) is known to be toxic and carcinogenic; it is widely used in dyeing nylon, woven fabrics, cotton textiles and wool textiles AR is a persistent pollutant in aquatic ecosystems, and prior studies have explored its degradation and removal using various adsorbents[3]. Because of its vibrant colour, high fixation rate, and robust colour fastness, the second biggest dyes are anthraquinone class of synthetic colourants and are frequently used to colour a variety of fabrics. In the textile business, Alizarin Red S is a common anthraquinone dye that has been widely utilised. ARS's fused aromatic structure makes it incredibly resistant to degradation, which is unfortunate because it poses a major risk to human health and the aquatic ecology. Therefore, ARS removal from dyeing wastewater has fascinated a lot of attention [4]. As a result, various techniques have been developed to treat water and wastewater containing toxic substances. These consist of oxidative degradation, photocatalytic degradation, biochemical degradation, adsorption, co-precipitation, electrocoagulation, and photodegradation [5]. Strontium hexaferrite is recognized in nanoscience device applications for its advantageous scientific properties, making it highly suitable for use as a ferrite material. Its strong electrical resistivity, corrosion resistance, chemical stability, and magnetic anisotropy make it ideal for this purpose. M-type hexaferrite finds wide applications in permanent magnets, telecommunications, high-density magnetic recording devices, magneto-optical systems, and microwave devices, owing to its excellent electrical and magnetic properties, complete chemical stability, high thermal endurance, and corrosion resistance. Additionally, strontium hexaferrite ($SrFe_{12}O_{19}$) combines intriguing chemical, physical, and magnetic characteristics with a high performance-to-cost ratio[6]. $SrFe_{12}O_{19}$, an n-type semiconductor, is widely used today as an effective photocatalyst for eliminating

toxic organic pollutants. Several synthesis methods, such as sol–gel, co-precipitation, hydrothermal, and microemulsion techniques, have been employed to produce $SrFe_{12}O_{19}$ [7]. Among these, the sol–gel method offers significant advantages, including precise stoichiometric control and favorable particle size distribution at relatively low temperatures [8].

Better control over particle size and shape is anticipated with sol-gel chemistry. Nevertheless, producing a homogenous precursor at ambient temperature does not ensure homogeneity throughout the reaction, which is why different sol–gel techniques have been developed to control or reduce phase isolation throughout synthesis. Interestingly, it is not always essential for the precursor to be entirely "random." Some of the most exciting recent advancements in the sol–gel field have emerged from gels that exhibit a certain level of ordering and structure [9]. Among the effective strategies for separating photoinduced electron–hole pairs, semiconductor coupling is gaining significant attention. This approach primarily involves forming a composite semiconductor material. By creating a coupled structure between a narrow-bandgap semiconductor and TiO_2 with aligned band potentials, the photosensitivity of TiO_2 can be extended into the visible spectrum. Under visible light excitation, photogenerated electrons or holes from the narrow-bandgap semiconductor can transfer to TiO_2, triggering a photocatalytic reaction. Consequently, combined photocatalysts often demonstrate excellent photocatalytic activity and have attracted substantial interest. Various coupling photocatalysts have been reported, including $ZnFe_2O_4/TiO_2$, $MnFe_2O_4/TiO_2$, $NiFe_2O_4/TiO_2$, and $CuFe_2O_4/TiO_2$[10].

When exposed to air, magnetic nanoparticles frequently struggle with aggregation-induced instability, which reduces their surface energy and makes them more vulnerable to oxidation. These nanoparticles become more dispersible and lose their magnetic characteristics as they cluster. Therefore, it is essential to develop novel techniques for chemically stabilising pure magnetic nanoparticles. According to research, silica (SiO_2) scoating magnetic nanoparticles successfully inhibits aggregation, oxidation of the magnetic core, and degradation. Furthermore, silica improves

photoinduced charge carrier transfer, and its porous structure raises surface area and adsorption capacity, which eventually boosts photocatalytic activity [11].

Materials based on graphene, such as graphene oxide (GO), have demonstrated great promise in eliminating new pollutants from water. GO may remove a wide range of toxins, including medications, personal care items, and chemicals that alter hormones, because of its huge surface area, which offers a large number of active sites for chemical reactions and a significant affinity for both organic and inorganic pollutants. Furthermore, GO is a versatile tool for water treatment since it may be altered to target particular impurities [12]. GO composites with various nanomaterials have demonstrated outstanding capacity for heavy metal ion removal. For example, GO-TiO_2-based adsorbents are effective in extracting divalent cadmium and zinc ions from wastewater, while silica-decorated GO nanocomposites (GO-Silica) are used to adsorb hazardous lead and mercury ions[13]. By serving as a support material and halting the leaching of fine metal oxide particles into treated water, graphene and metal oxides extend the adsorbent's lifespan. This combination also enhances the mechanical strength and durability of the adsorbent. Various interaction modes between graphene/metal oxide composites and different pollutant types further contribute to their effectiveness in water purification[14].

To address this band gap in the literature, a novel $SrFe_{12}O_{19}/TiO_2/SiO_2$/GO hybrid material was proposed and synthesized via Sol-gel method and Hummers' process. The resulting $SrFe_{12}O_{19}/TiO_2/SiO_2$/GO material was comprehensively characterized, focusing on its morphology as well as its magnetic properties. This study represents the first investigation into the photocatalytic activity of Strantium spinel-ferrite-based materials in degrading organic dyes. A possible photocatalytic mechanism for the degradation of organic dyes by hybrid materials is $SrFe_{12}O_{19}/TiO_2/SiO_2$/GO proposed and analyzed.

2. Materials and Methods

The synthesis of the $SrFe_{12}O_{19}/TiO_2/SiO_2$/GO nanocomposite utilized the following chemicals: tetraethyl orthosilicate, ethylene glycol, strontium nitrate, ferric citrate,

citric acid, titanium tetrachloride, hydrochloric acid, phosphoric acid, potassium permanganate, hydrogen peroxide, and sulfuric acid. All compounds were analytical grade and were utilised exactly as received, without any further purification. Deionized water was used in all reactions.

2.1 Synthesis of $SrFe_{12}O_{19}$ nanoparticle: First, a strontium nitrate solution is prepared by dissolving 4.23 grams of strontium nitrate in 10 milliliters of distilled water, while a ferric citrate solution is made by dissolving 71.64 grams of ferric citrate in 10 milliliters of distilled water. These solutions are combined in a beaker, and 12.6 grams of citric acid are added. The solution's pH is gradually adjusted to neutrality by adding ammonia. Subsequently, 20 milliliters of ethylene glycol are introduced. The solution is then heated for two hours on a hot plate until a dry powder forms, followed by calcination at 800 °C to yield fine strontium ferrite nanopowder.

2.2 Synthesis of Nano TiO_2: In a beaker covered with aluminum foil, 350 mL of distilled water having 0.5 mL of HCl solution was gradually mixed with 6.9 g of $TiCl_4$. After one hour of magnetic stirring, a white, curd-like precipitate formed in the beaker. The mixture was then heated on a hot plate to a temperature between 80 and 100 °C. After the fine powder formed, it was dried in a hot air oven set to 80 °C. Finally, the dried powder was ground with a mortar and pestle and calcined at 400 °C for two hours [15].

2.3 Synthesis of SiO_2: A tetraethyl orthosilicate (TEOS) solution was prepared by mixing 0.3 moles of ethanol with TEOS. To prepare the ammonia solution, 0.1 to 0.75 moles of ammonia were combined with 0.25 to 2.0 moles of additional ethanol. After drying at 80 °C for six hours and calcining at 900 °C for two hours, the two solutions were combined and vigorously stirred for thirty minutes.

2.4 Synthesis of GO: Graphene oxide (GO) was synthesized from pure graphite powder using a modified Hummers' method. Firstly, 27 mL of sulfuric acid (H_2SO_4) and 3 mL of phosphoric acid (H_3PO_4) were combined in a 9:1 volume ratio and stirred briefly. Next, 0.225 grams of graphite powder were added to the acid mixture with

continuous stirring. Subsequently, 1.32 grams of potassium permanganate ($KMnO_4$) were slowly added. After six hours of stirring, the solution turned dark green. To eliminate excess $KMnO_4$, 0.675 mL of hydrogen peroxide (H_2O_2) were gradually introduced, and the mixture was agitated for ten minutes. After the exothermic reaction, the solution was allowed to cool. Finally, 30 mL of deionized water (DIW) and 10 mL of hydrochloric acid (HCl) were added [16].

2.5 Synthesis of $SrFe_{12}O_{19}/TiO_2/SiO_2$/GO Nanocomposite: The $SrFe_{12}O_{19}/TiO_2/SiO_2$/GO nanocomposite was synthesized by incorporating 10% GO. For preparing the $SrFe_{12}O_{19}/TiO_2/SiO_2$-10% GO nanocomposite, 1 mL of 10% graphene oxide was added to 20 mL of deionized water and sonicated in an ultrasonic bath for 30 minutes. Following this, 1 gram of $SrFe_{12}O_{19}/TiO_2/SiO_2$ was dispersed into the GO solution, which was then sonicated for an additional 30 minutes. The mixture was continuously stirred for approximately 4 hours. The resulting brown product was gathered and dried in a hot air oven at 80 °C for 2 hours.

3. Instrumentation:

The synthesised nanocomposites were characterized using a range of techniques. The photocatalysts were evaluated using X-ray diffraction (XRD) on a Bruker DX-5 diffractometer with a proportional counter and Cu Kα radiation (λ = 1.54 Å) to assess their quality and crystallite size. Scanning electron microscope (SEM) images were taken with a Carl Zeiss Gemini 300 (Germany) to evaluate surface morphology, and transmission electron microscopy (TEM) was used to determine form and demonstrate particle size.

The vibrational modes of the composite materials were examined using Fourier transform infrared (FTIR) spectroscopy on an IR Prestige 21 spectrometer. Spectra were gathered in the range of 500 to 4000 cm^{-1}. UV-Vis diffuse reflectance spectroscopy (DRS) was used to study the structural and band gap properties of the composite. Measurements were done on a Shimadzu 2600R using $BaSO_4$ as a reference spanning the wavelength range of 200–800 nm. The magnetic characteristics of

the photocatalyst composite were evaluated at room temperature via a vibrating sample magnetometer (VSM).

4. Results and Discussion

4.1 UV-VIS DRS Analysis and Band Structure Determination: The optical properties and band gap energy of the fabricated $SrFe_{12}O_{19}$–TiO_2–SiO_2–GO nanocomposite were investigated using UV-VIS diffuse reflectance spectroscopy (DRS), as illustrated in the figure. The sample shows distinct absorption at 450 nm, indicating the formation of the hexagonal phase and confirming a well-defined crystalline lattice structure. The DRS data, in conjunction with the Kubelka–Munk (K–M) model, was used to estimate the band gap energy (BE) of the samples, as depicted in Fig 1. The calculated band gap energy for the $SrFe_{12}O_{19}$–TiO_2–SiO_2–GO composite is 2.29 eV. This band gap value, being below 3 eV, suggests high solar energy utilization efficiency and strong potential for photocatalytic applications.

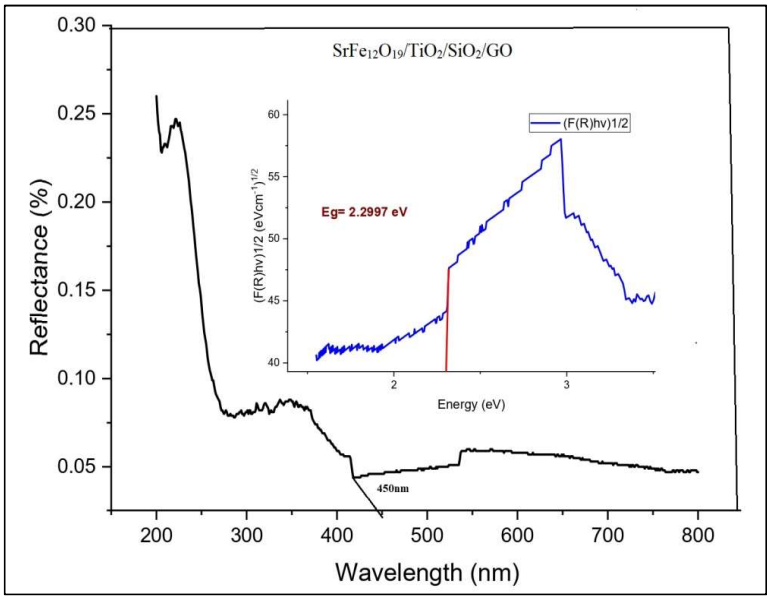

Fig.1. UV-Visible diffuse reflectance spectra of $SrFe_{12}O_{19}$ / TiO_2/SiO_2 /GO

4.2 X-ray Diffraction Studies: The X-ray diffraction (XRD) pattern of the $SrFe_{12}O_{19}$–TiO_2–SiO_2–GO nanocomposite photocatalyst is displayed in Figure 2. The average crystallite size (D) and the experimentally observed intense diffraction peaks were matched and indexed using JCPDS Card Nos. 84-1531, 021-1272, and 00-041-148710 for $SrFe_{12}O_{19}$, TiO_2, and GO in the anatase and spinel phases, respectively. In Figure 2, sharp and intense peaks for the GO–$SrFe_{12}O_{19}$ component appear at 2θ values of 10°, 25°, 34°, 35°, 55°, and 57°, corresponding to the planes (001), (101), (107), (114), (105), and (2011). These XRD planes (001), (107), (114), and (2011) confirm that GO and $SrFe_{12}O_{19}$ are the primary phases, emphasizing the crystalline nature of the sample. Due to its amorphous nature, the SiO_2 peak is not visible, while the TiO_2 photocatalyst peaks at 2θ values of 25° and 55° correspond to the (101) and (105) planes, alongside the peaks and planes of $SrFe_{12}O_{19}$, TiO_2, and GO in the XRD pattern. The crystallite sizes of $SrFe_{12}O_{19}$, SiO_2, TiO_2, and GO were calculated using the Scherrer formula. This analysis confirms the successful formation of the composite, with strontium ferrite presenting a cubic spinel structure and TiO_2 existing in the anatase crystalline phase, consistent with recent literature.

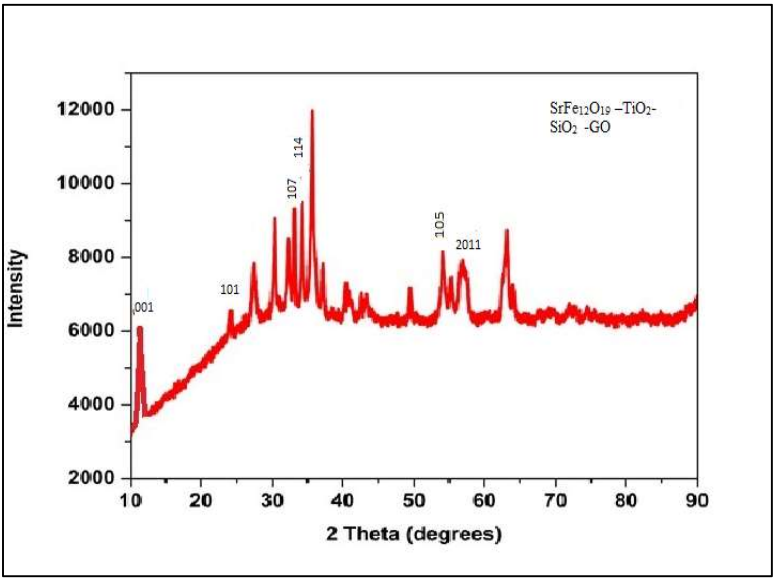

Fig.2. pattern of $SrFe_{12}O_{19}$ / TiO_2/SiO_2 /GO XRD

4.3 FTIR Analysis: The FT-IR spectra of the examined samples are presented in the figure. The primary bands between 3848 and 2355 cm^{-1} correspond to the vibrations of hydroxyl groups, including the hydrogen-bonded –OH···H at 3677 cm^{-1}, the isolated –OH in TiO_2 and $SrFe_{12}O_{19}$ at 3789 cm^{-1}, and the isolated silanol groups (≡SiOH) also at 3789 cm^{-1}. Among the SiO_2-containing samples, the one exhibiting the highest band intensity has isolated –OH groups. In contrast, samples without silica do not show these bands, while the samples containing TiO_2 and $SrFe_{12}O_{19}$ display bands for isolated hydroxyl groups that shift to lower wavenumbers (3677 cm^{-1}). The peaks around 3677 cm^{-1} indicate the presence of hydrogen-bonded SiOH–OSi groups, specifically internal hydroxyl groups. A broad band peaking around 3359 cm^{-1} is attributed to physically adsorbed water and the hydrogen-bonded –OH···H groups within the oxide structures. In the spectra of the silica-containing samples, the broad, intense bands in the range of 1418–1101 cm^{-1} are linked to the asymmetric stretching vibrations of Si–O–Si bridges, while the peaks near 530 cm^{-1} and 470 cm^{-1} correspond to the symmetric stretching and deformation modes of Si–O–Si, respectively. Additionally, a band observed at 1720 cm^{-1} is assigned to the carboxyl group, and the broad peak at 3359 cm^{-1} agrees to the stretching mode of the O–H bond.

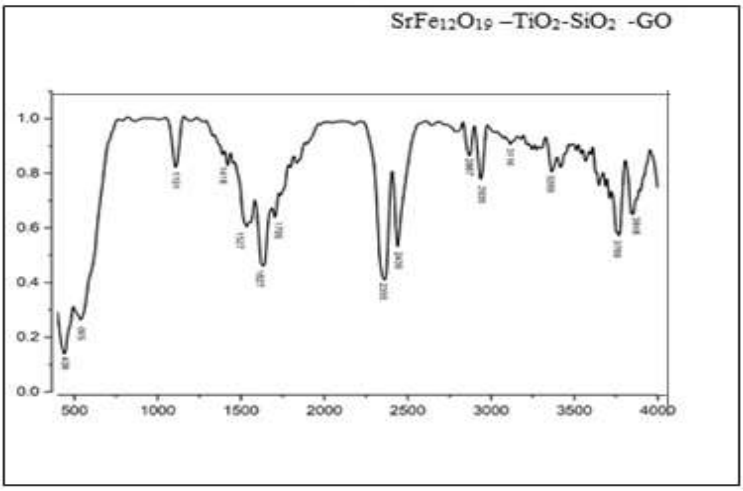

Fig.3. FTIR of $SrFe_{12}O_{19}$/ TiO_2/SiO_2 /GO

4.4 SEM and EDS Analysis: Scanning electron microscopy (SEM) was active to investigate the structural morphology of the $SrFe_{12}O_{19}$–TiO_2–SiO_2–GO photocatalysts and nanocomposite. Figure 4 displays the SEM images, which reveal predominantly spherical nanoparticles. However, the $SrFe_{12}O_{19}$–SiO_2 sample exhibited a significant degree of aggregation and varied surface morphologies, likely due to the magnetic attraction between the strontium ferrite and silica layers. In contrast, the $SrFe_{12}O_{19}$–TiO_2–SiO_2–GO sample showed a heterogeneous structure characterized by a high degree of surface roughness, a feature absent in the pristine TiO_2 photocatalyst. The images also indicate the presence of spherical nanoparticles alongside some aggregates of TiO_2, possibly resulting from the hydrolysis of titanium dioxide. Additionally, Figure 4 presents the energy-dispersive X-ray spectroscopy (EDS) spectrum of the $SrFe_{12}O_{19}$/SiO_2/TiO_2/GO nanostructures, confirming the presence of elements Si, Fe Sr, O, C, and Ti. These findings suggest that the sample precursors were prepared as intended, thereby incidently confirming the successful formation of the composite.

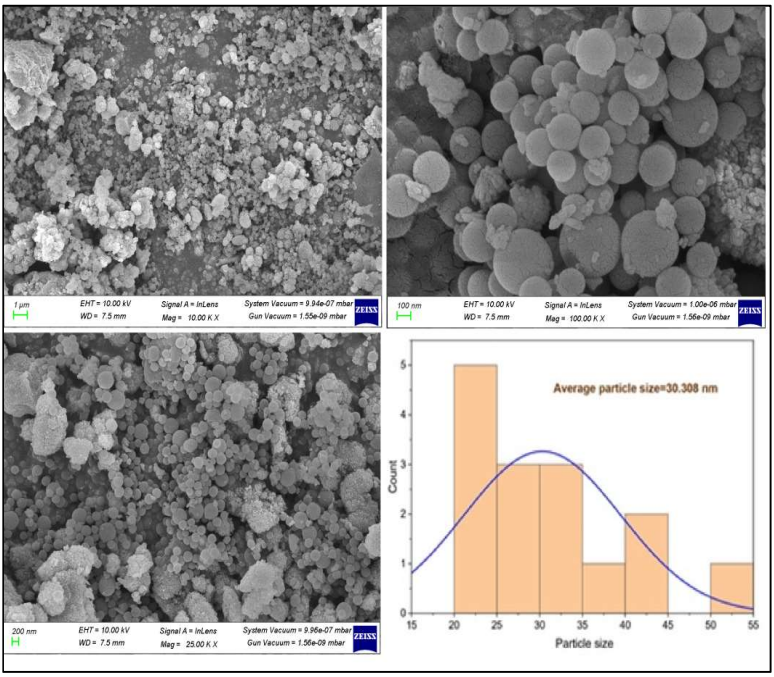

Fig. 4. SEM images of $SrFe_{12}O_{19}$/ TiO_2/SiO_2 /GO a) 1µm b)100nm c)200nm d) Particle size distribution of $SrFe_{12}O_{19}$/ TiO_2/SiO_2 /GO

4.5 TEM Analysis: Transmission Electron Microscopy (TEM) characterization of $SrFe_{12}O_{19}$–TiO_2–SiO_2–GO (Strontium hexaferrite, Titanium dioxide, Silicon dioxide, and Graphene oxide) nanocomposites provides detailed insight into the structural, morphological, and compositional features of the material. TEM allows for visualization of the size and shape of $SrFe_{12}O_{19}$, TiO_2, and SiO_2 nanoparticles within the composite, aiding in the analysis of particle distribution and uniformity, which are essential for the material's magnetic and photocatalytic properties. The morphology of the graphene oxide sheets, including their thickness, lateral dimensions, and interaction with other nanoparticles, can also be observed. High-resolution TEM (HRTEM) further enables the identification of the crystalline structure of the $SrFe_{12}O_{19}$, TiO_2, and SiO_2 phases. Lattice fringes in HRTEM images reveal crystallographic orientation and can detect any lattice defects. Additionally, TEM analysis allows examination of

the interfaces between components ($SrFe_{12}O_{19}$, TiO_2, SiO_2, and GO), providing insight into nanoscale bonding and interactions.

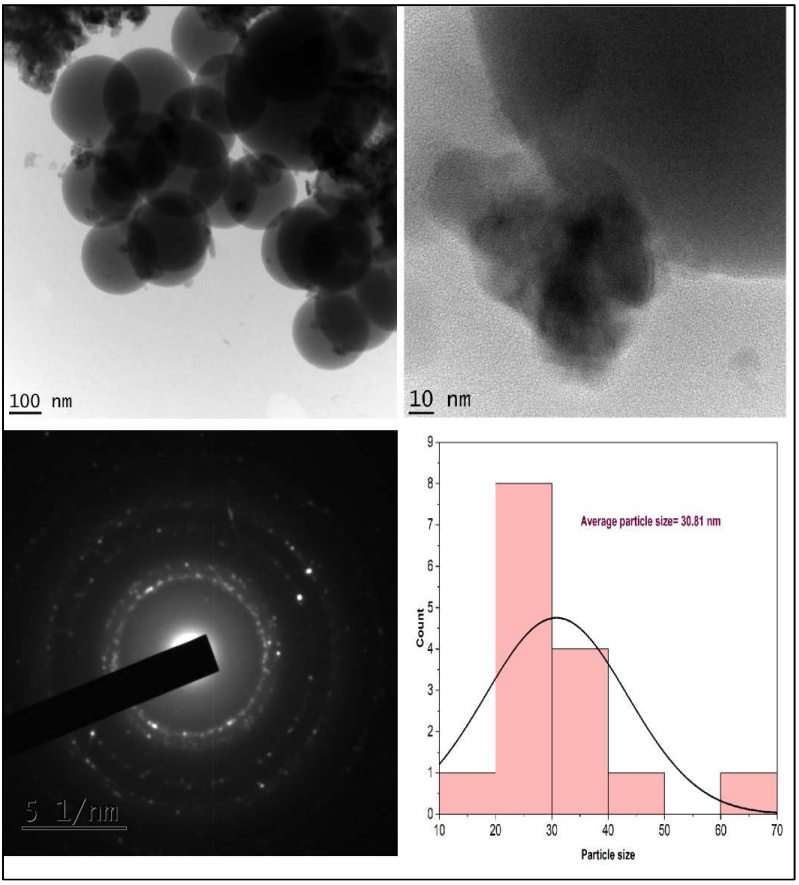

Fig 5. TEM images of $SrFe_{12}O_{19}$/ TiO_2/SiO_2 /GO a)100nm b)10nm c)100nm d)) Particle size distribution of $SrFe_{12}O_{19}$/ TiO_2/SiO_2 /GO

4.6 Magnetic Property Analysis: The magnetic properties of the sample were assessed using a vibrating sample magnetometer (VSM) at room temperature. The hysteresis loop for the magnetic $SrFe_{12}O_{19}$–TiO_2–SiO_2–GO nanoparticles, synthesized via the sol-gel and modified Hummers' methods, shows superparamagnetic behavior. The nanoparticles exhibit a saturation magnetization of 80 emu/g and a coercivity approaching zero Oe, indicating minimal resistance to demagnetization. This level of

magnetization is sufficient for magnetic recycling applications, making these nanoparticles suitable for use as recyclable cores in catalysts for environmental purposes. The composite's magnetic properties are largely attributed to $SrFe_{12}O_{19}$, with the coercivity close to zero suggesting easy reversibility of magnetization. Thus, the $SrFe_{12}O_{19}$–TiO_2–SiO_2–GO nanocomposite serves as a regenerable and reusable magnetic heterogeneous catalyst, ideal for sustainable applications.

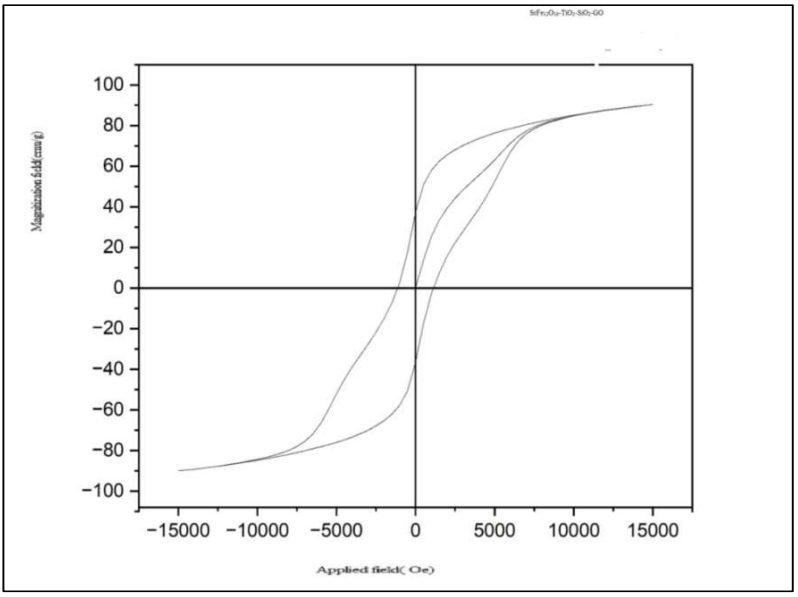

Fig. 6. Magnetization loop for $SrFe_{12}O_{19}/TiO_2/SiO_2$/GO composite at room temperature

5. PHOTOCATALYTIC ACTIVITY

5.1. Photocatalytic Activity Evaluation: The photocatalytic performance of the synthesized sample was assessed by degrading Alizarin red in aqueous solutions. A 300W xenon lamp emitting a broad spectrum of UV and visible light served as the light source. The reactions were conducted in a 200 ml reactor (40 mm height, 85 mm diameter) with continuous stirring. The STSG photocatalyst was employed for the degradation of Alizarin red, initially prepared at a concentration of 10.0 mg/l. Before irradiation, the solution containing the photocatalyst were agitated in the dark to reach adsorption equilibrium, ensuring stable concentration. After irradiation, 5.0 ml sam-

ples were taken at intervals, centrifuged to remove the photocatalyst, and the supernatant was examined using a UV-Vis spectrophotometer at 510 nm.(The best photocatalytic degradation efficiency for zero charge (pH 7) and basic pH is for AR, 98.21% and 68.38%, MR 33.01% and 17.52%, BPB 73.17% and 17.52%, MB 72.32% and 76.81%, and MG 85.59% and 86.93%, respectively, under UV light irradiation for 35 min- AR shows percentage of degradation in previous paper report).

5.2. Effect of Initial Dye Concentration: The influence of initial Alizarin red dye concentration on the photocatalytic performance of the $SrFe_{12}O_{19}/TiO_2/SiO_2/GO$ composite was evaluated by varying the starting AR dye concentration from 5 to 100 ppm at a fixed solution pH of 6 and a catalyst loading of 10 mg/L. As shown in Fig., at a 10 mg/L AR dye concentration, the maximum degradation rate (100%) was achieved within 110 minutes. The observed decrease in degradation rate with higher AR dye concentrations is attributed to the "blanket effect," where AR dye molecules occupy active sites on the catalyst surface, thereby hindering OH radical production. Additionally, despite a constant catalyst dosage of 10 mg/L, the generation of reactive species (notably OH radicals) does not scale proportionally to match the increased amount of AR dye molecules. The AR dye's light-filtering effect further contributes to the reduced degradation rate. Regression coefficients and rate constants for the photocatalyst were assessed under various optimized reaction conditions. Adjusting each reaction parameter individually led to increased rate constants for AR dye degradation, confirming that at 10 mg/L, pH 6, $SrFe_{12}O_{19}/TiO_2/SiO_2/GO$ acts as an efficient photocatalyst for AR dye breakdown in a 10 ppm solution.

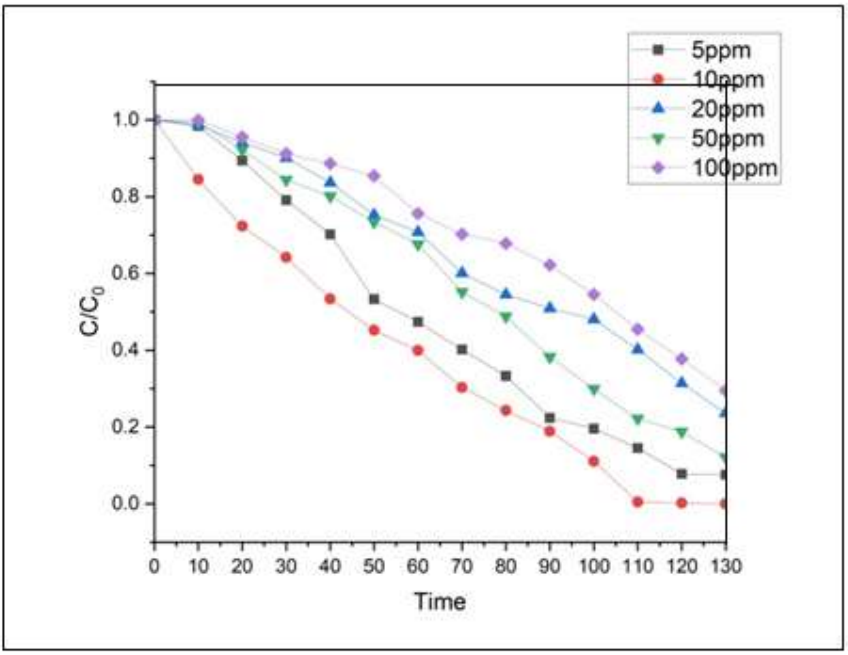

Fig.7. Effect of dye concentration on $SrFe_{12}O_{19}/TiO_2/SiO_2/GO$

5.3 Effect of pH: Due to the complex nature of industrial wastewater, the photocatalytic degradation of pollutants varies depending on the solution's pH. The pH of the $SrFe_{12}O_{19}/TiO_2/SiO_2/GO$ nanocomposite solution was adjusted from 4 to 8 by adding a 0.1M HCl or NaOH solution. When 10 mg/L of the nanocomposite was introduced into an aqueous solution containing AR dye, the pH of the $SrFe_{12}O_{19}/TiO_2/SiO_2/GO$ solution was initially measured as 4. Adsorption experiments across different pH levels revealed that at pH 6, after 90 minutes of irradiation, the nanocomposite achieved maximum adsorption and 100% degradation, as shown in Fig. As the pH increased to 6, the degradation rate initially rose but then gradually decreased. At lower pH values, the catalyst surface acquires a more negative charge, influencing adsorption and photocatalytic activity.

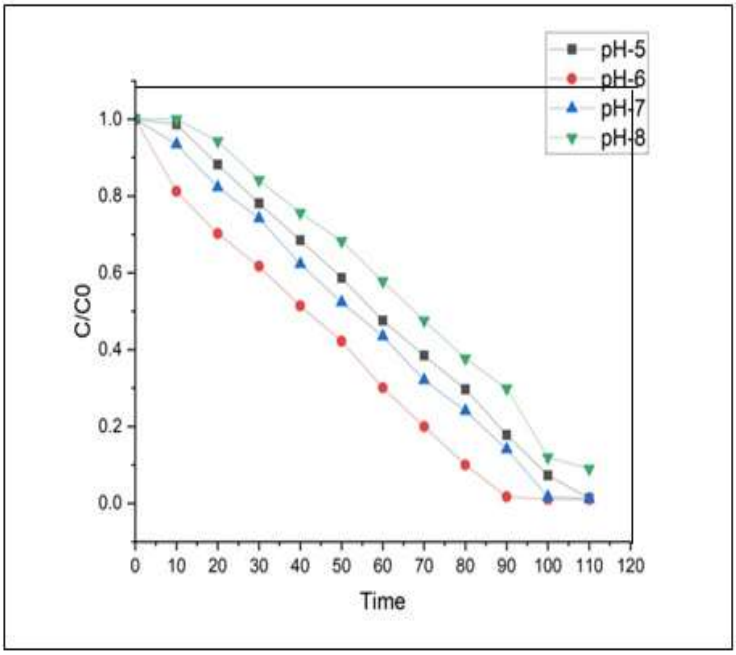

Fig. 8. Effect of pH on $SrFe_{12}O_{19}/TiO_2/SiO_2/GO$

5.4 Effect of Temperature: Limited research has explored the impact of temperature on photocatalysis, yet recent findings suggest that environmental temperature plays a crucial role in the photodegradation of AR dye. Increasing the temperature from 30 °C to 40 °C can enhance photocatalytic efficiency by roughly two to three times. Since UV light is a component of solar energy, it not only initiates the photocatalytic process but also raises the temperature of the photocatalytic system. The study showed that temperatures below 40 °C alone are insufficient for pyrolysis or self-degradation of the dye through radiation absorption. Effective degradation was achieved when both $SrFe_{12}O_{19}/TiO_2/SiO_2/GO$ and UV radiation were applied, as depicted in Fig., underscoring the $SrFe_{12}O_{19}/TiO_2/SiO_2/GO$ nanocomposite's utility as an efficient photocatalyst.

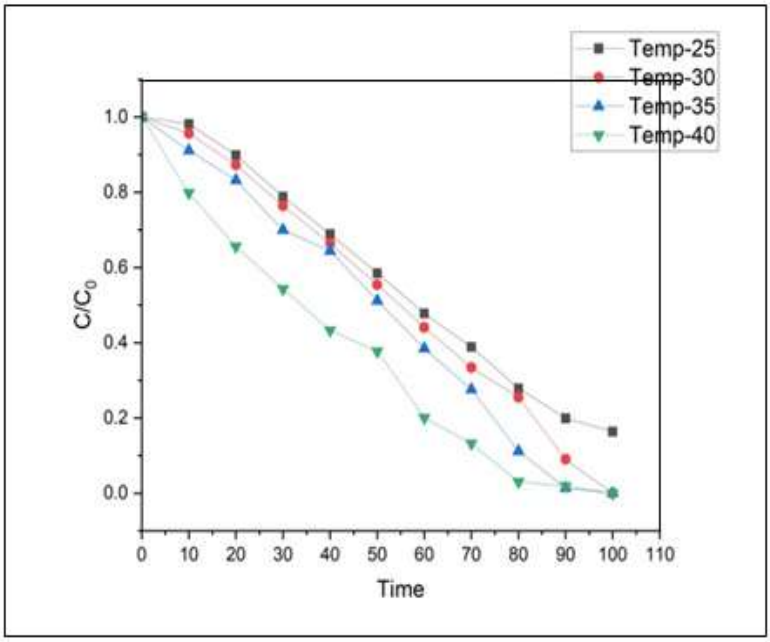

Fig. 9. Effect of Temperature on $SrFe_{12}O_{19}/TiO_2/SiO_2/GO$

5.5 Effect of Catalyst Dosage: To investigate the effect of nanocomposite concentration on the photocatalytic degradation of AR dye, the concentration of the synthesized composite was varied from 0.20 g/L to 0.50 g/L, maintaining a constant solution pH of 6 and an initial AR dye concentration of 10 mg/L. This experiment aimed to understand how the concentration of the nanocomposite affects the photocatalytic degradation of AR dye under visible light. As illustrated in the figure, the degradation rate of AR dye increased with higher composite loading, reaching an optimum at 0.40 g/L. This improvement in degradation rate can be attributed to the larger total surface area and increased number of available active sites. However, with further increases in composite loading, the degradation rate declined, likely due to catalyst dispersion, which reduces the number of active sites accessible to light. Additionally, higher solution turbidity at increased loading levels further reduces light penetration.

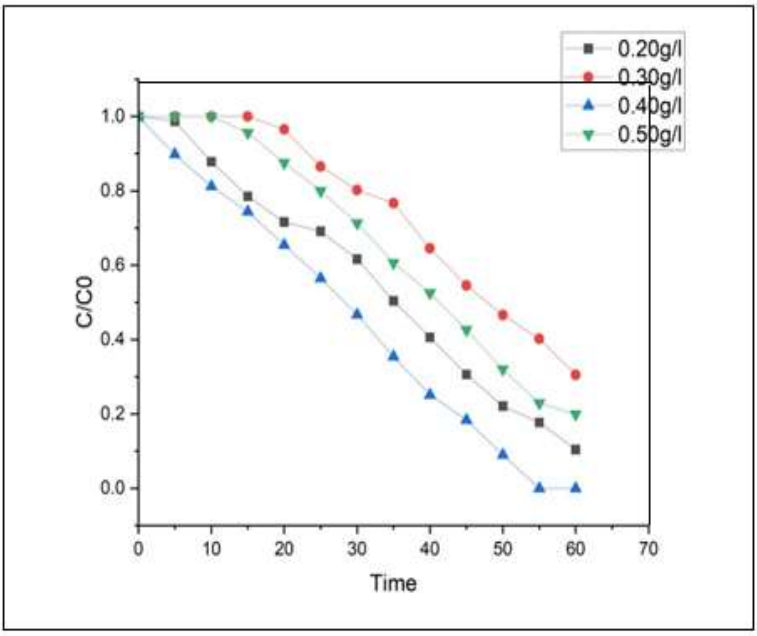

Fig. 10. Effect of catalyst dosage on $SrFe_{12}O_{19}/TiO_2/SiO_2/GO$

5.5 Effect of Irradiation Time: It is important to note that exposure to visible light can photoexcite AR, the model pollutant. To eliminate any influence of the dye itself on the evaluation of the material's catalytic activity, additional photodegradation tests were conducted using AR dye under solar radiation. The absorbance of AR solutions under visible light at various irradiation times is shown in Fig. Over the irradiation period, the absorption peaks of AR steadily decrease and nearly disappear after 90 minutes. After this 90-minute exposure, the degradation rates for AR are 93.9%, 87.2%, and 87.2%, respectively. Fig. also presents images of the AR solutions' color change during degradation. The ferrite-coated TiO_2, prepared at pH 6, catalyst concentration of 0.40 g/L, and temperature of 40 °C, is demonstrated to be an effective semiconducting photocatalytic material with a notable ability to degrade AR, as evidenced by all data provided. A compilation of previous reports on band gaps and the activity of TiO_2-doped photocatalytic materials by various researchers

supports this finding. To the best of our knowledge, ferrite-doped materials show enhanced photodegradation activity.

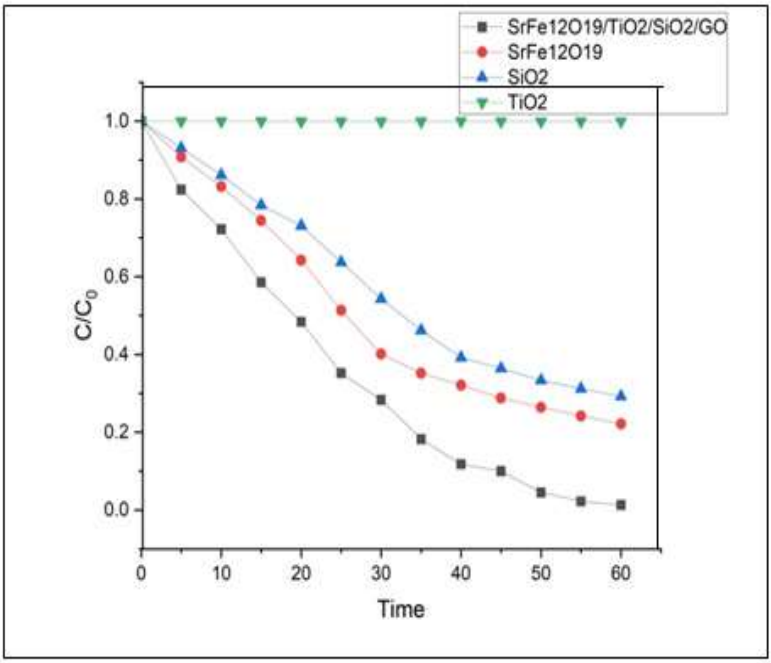

Fig.11. Irradiation time on $SrFe_{12}O_{19}/TiO_2/SiO_2/GO$

5.6 Reusability of photocatalyst: Lastly, the stability and reusability of the top-performing photocatalyst, $SrFe_{12}O_{19}/TiO_2/SiO_2/GO$ were evaluated at an optimal concentration of 0.40 mg/L. A key aspect of heterogeneous catalysis with significant industrial interest is the catalyst's reusability. Typically, reusing catalysts involves separating them from the reaction medium through filtration or centrifugation, then regenerating them by washing with suitable liquids or heat treatment to remove surface intermediates that can cause deactivation. These lengthy and complex procedures contribute to higher processing costs. In this study, we demonstrate that the catalyst can be reused directly, without washing or removal from the reaction medium. The initial dye concentration of 10 ppm was restored by adding the necessary amount of AR dye into the faded solution. Cycling experiments were conducted under the same

reaction conditions to monitor AR concentration over multiple uses. Results (Figure) indicate a moderate decline in the activity of the oxygen-deficient nanocomposite, decreasing from 98% degradation in the first cycle to 93.4% in the second and 75.9% in the third cycle, within 50 minutes of exposure.

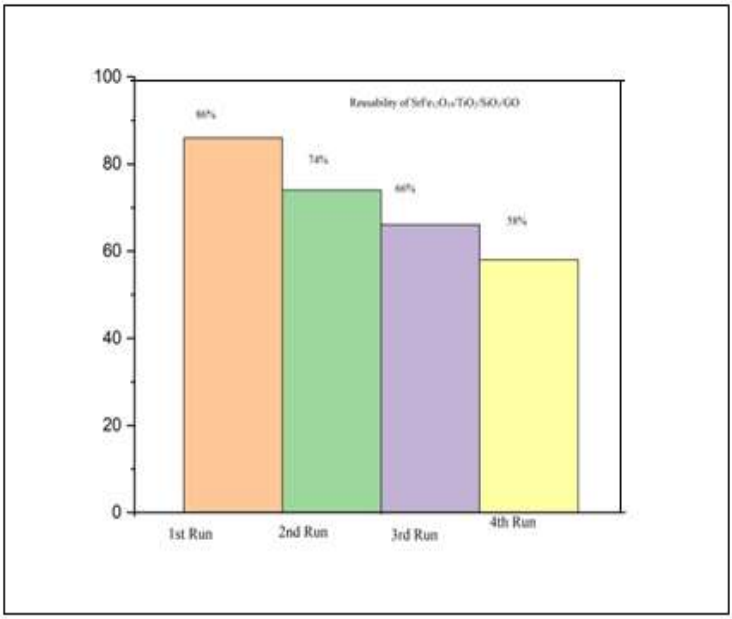

Fig.12. Reusability of $SrFe_{12}O_{19}/TiO_2/SiO_2/GO$

6. Antibacterial activity

The antibacterial activity of the $SrFe_{12}O_{19}/TiO_2/SiO_2/GO$ nanocomposite was evaluated against *Pseudomonas aeruginosa* (ATCC-15692) and *Micrococcus luteus* (ATCC 9341) using the agar disc diffusion method. The pathogenic bacterial isolates were pre-cultured in nutrient broth medium at 37 °C, shaken at 120 rpm, and incubated overnight. Nanocomposite samples were prepared at concentrations of 20, 60, and 100 µg/mL. Müller–Hinton agar was used for the subculturing of pure bacterial cultures. Wells approximately 4 mm deep were created in the Agar, and 60 µL of the nanocomposite solutions were added to each well using a micropipette. Tetracycline served as the control. The plates were incubated at 37 °C for about 24

hours, and the zones of inhibition were measured to assess antibacterial activity. The nanoparticles and nanocomposite were evaluated at three different concentrations, and their antibacterial activity was compared to that of tetracycline (25 µg/mL). The bacterial toxicity was assessed against two pathogens, *Pseudomonas aeruginosa* (ATCC-15692) and *Micrococcus luteus* (ATCC 9341). Figure 13 presents the toxicity results as inhibition zones measured in millimeters.

Interestingly, the synthesized $SrFe_{12}O_{19}/TiO_2/SiO_2/GO$ ferrite-based metal oxide exhibited minimal toxic effects, whereas the magnetic photocatalyst $SrFe_{12}O_{19}/TiO_2/SiO_2/GO$ nanocomposite demonstrated significant toxicity at varying concentrations against *Pseudomonas aeruginosa* (ATCC-15692) and *Micrococcus luteus* (ATCC 9341). At a concentration of 20 µg/mL, the $SrFe_{12}O_{19}/TiO_2/SiO_2/GO$ nanocomposite showed marked antibacterial activity, with inhibition zones of 14 mm and 15 mm, respectively. At 60 µg/mL, the nanocomposite exhibited enhanced antibacterial performance, with inhibition zones of 18 mm against *Pseudomonas aeruginosa* (ATCC-15692) and 17 mm against *Micrococcus luteus* (ATCC 9341). The highest toxicity levels were recorded for the $SrFe_{12}O_{19}/TiO_2/SiO_2/GO$ nanocomposite, with inhibition zones of 17 mm and 19 mm, respectively. The results highlight the synergistic antibacterial activity of the $SrFe_{12}O_{19}/TiO_2/SiO_2/GO$ nanocomposite, aligning with findings reported in the literature. The $SrFe_{12}O_{19}/TiO_2/SiO_2/GO$ nanocomposite exhibited antibacterial effects specifically in solution 3, effectively killing both Gram-positive and Gram-negative bacteria. However, under light exposure, all three solutions at different concentrations displayed antibacterial activity, albeit to varying extents. This phenomenon is attributed to the light-induced excitation of the composite, leading to the generation of reactive oxygen species (ROS) in the solution. These ROS enhance bacterial killing by promoting oxidative damage. Consequently, the nanostructured $SrFe_{12}O_{19}/TiO_2/SiO_2/GO$ composite induces significant mechanical damage to the bacterial cell wall and disrupts bacterial functions, resulting in an improved bactericidal effect.

Table.1: Zone of inhibition values obtained from the Antibacterial activity of $SrFe_{12}O_{19}/TiO_2/SiO_2/GO$

S.NO	Sample	Concentration(µg/ml)	*Micrococcus luteus*(ATCC 9341) (gram positive) mm	*Pseudomonus aeruginosa* (ATCC-15692) (gram negative) mm
A	$SrFe_{12}O_{19}/TiO_2/SiO_2/$ GO synthesized	20	2	3
		60	2	3
		100	3	4
	Tetracycline	25	18	21
B	$SrFe_{12}O_{19}/TiO_2/SiO_2/GO$ nanocomposite/ Tetra-cycline	20	14	15
		60	17	18
		100	17	19
	Tetracycline	25	21	23

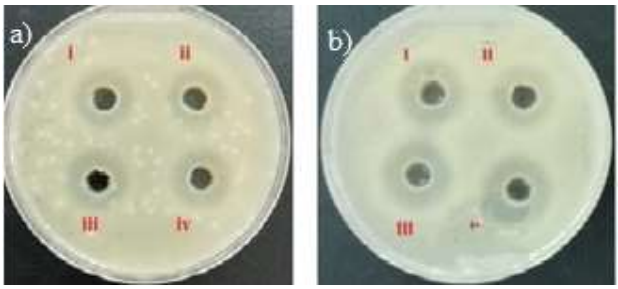

Fig.13. (a), (b) are the Images of the $SrFe_{12}O_{19}/TiO_2/SiO_2/GO$ nanocomposite inhibition zones against two types of pathogenic bacterial.

7. Conclusion:

The work presents the nanocomposite magnetic photocatalyst $SrFe_{12}O_{19}/TiO_2/SiO_2/GO$ nanocomposite was synthesized using the sol-gel method and Hummers method. The characterization results obtained through UV-DRS, XRD, FTIR, SEM, TEM, and VSM indicate that is $SrFe_{12}O_{19}/TiO_2/SiO_2/GO$ a good photo-catalyst and a reusable, easily separable magnetic composite A novel nanophotocatalyst, $SrFe_{12}O_{19}/TiO_2/SiO_2/GO$ was synthesized with enhanced sunlight-driven activity, achieving 100% degradation of Alizarin red dye in aqueous solution within 60 minutes. The catalyst demonstrated excellent reusability with minimal loss in activity over multiple cycles. Additionally, reactive Alizarin red dye was mineralized up to 70% over a 5-hour period. These results suggest that $SrFe_{12}O_{19}/TiO_2/SiO_2/GO$ holds great potential as a nanophotocatalyst for wastewater treatment applications.The addition of graphene oxide (GO) further boosts the material's photocatalytic performance by improving electron mobility, reducing charge recombination, and extending the absorption spectrum into the visible region. This synergy makes $SrFe_{12}O_{19}/TiO_2/SiO_2/GO$ a highly effective photocatalyst for applications such as wastewater treatment, where it can degrade persistent organic pollutants and disinfect harmful pathogens under sunlight or artificial light. Looking ahead, $SrFe_{12}O_{19}/TiO_2/SiO_2/GO$ composites can play a pivotal role in sustainable energy production, particularly in hydrogen generation via photocatalytic water splitting. The high charge separation efficiency and visible-light activity of these composites make them suitable for practical solar-to-hydrogen conversion systems. Additionally, they could be utilized in air purification, carbon dioxide reduction, and advanced oxidation processes to mitigate environmental pollution. With further optimization in synthesis techniques, such as doping and defect engineering, and scalable production methods, these materials can become cost-effective and widely applicable. Their integration into real-world systems, such as self-cleaning surfaces, energy-efficient coatings, and decentralized water purification devices, marks a significant step toward greener technologies.

8. Acknowledgements:

The authors extend their gratitude to Andhra University, Visakhapatnam, India, specifically the Advanced Analytical Laboratory, for providing spectral analysis support. The authors declare no conflicts of interest concerning the publication of this article.

9. Declaration: The authors declare no competing interest.

10. References:

1. Robert Liu, H. T. Ou.Synthesis and Application of Magnetic Photocatalyst of Ni-Zn Ferrite/TiO_2 from IC Lead Frame Scraps, 2015 https://doi.org/10.1155/2015/727210.
2. Hellen C. T. Firminoa,b, Emanuel P. Nascimentoa,b, Rondinele N. Araujoa,b, Francisco J.A. Loureiroc, Gelmires A. Nevesa,b, Marco A. Moralesd , Romualdo R. Menezesa,b Nickel ferrite/TiO_2 Nanofibrous Composite: Enhanced Photocatalytic Dye Degradation Under Visible Light 2024 https://doi.org/10.1590/1980-5373-MR-2023-0391.
3. Shivani S. Vedula1 · Ganapati D. Yadav1Treatment of wastewater containing alizarin red dye: development and application of magnetic chitosan as a natural eco-friendly material , Clean Technologies and Environmental Policy (2023) 25:865–878 https://doi.org/10.1007/s10098-022-02408-9.
4. . Zhifeng Zhang∗ , Huijuan Chen, Wenmei Wu, Wenting Pang, Guiqin Yan Efficient removal of Alizarin Red S from aqueous solution by polyethyleneimine functionalized magnetic carbon nanotubes ,Bioresource Technology ,Volume 293, December 2019, 122100 https://doi.org/10.1016/j.biortech.2019.122100.
5. https://doi.org/10.3390/pr9040589 Khadijah Mohammedsaleh M Katubi Norah Salem Alsaiari Fatimah Mohammed Alzahrani ,Saifeldin M. Siddeeg [2,3] andn Mohamed A. Tahoon, Synthesis of Manganese Ferrite/Graphene Oxide Magnetic Nanocomposite for Pollutants Removal from Water 2021, *9*(4), 589; https://doi.org/10.3390/pr9040589.
6. Jesurani.S, Srimeena .S, and Thameem Fathima K Preparation and Characterization of SrFe12O19/ZrO2Nanocomposite by using Sol-Gel method Int. J. Adv. Res. 5(11), 1068-1074 International journal of advance research https://dx.doi.org/10.21474/IJAR01/5867.
7. Dalal A. Alshammari An insight into Cu/Gd co-doping and MWCNTs modifcation on SrFe12O19 for efective removal of industrial efuents 2024 https://doi.org/10.1007/s11581-024-05773-1.
8. Rita Sundari, Tang Ing Hua, Madzlan Aziz, Umar Kalmar Nizar the characterization study of ferrites (magnesium and manganese) using sol gel method (Kajian

Pencirian untuk Ferit (Magnesium dan Mangan) Menggunakan Kaedah Sol Gel) ,The Malaysian Journal of Analytical Sciences, Vol 18 No 3 (2014): 485 – 490.

9. A. E. Danks, S. R. Hall and Z. Schnepp The evolution of 'sol–gel' chemistry as a technique for materials synthesis,2019 **https://doi.org/10.1039/C5MH00260E.**
10. Zhang , Yiming He, Tinghua W, Photocatalytic degradation of RhB over $MgFe_2O_4/TiO_2$ composite materials , Materials Science and Engineering: B Volume 176, 2011, Pages 1497-1500, 18 https://doi.org/10.1016/j.mseb.2011.09.022.
11. Ajaypal Kaur , Manpreet Kaur , Vasundhara Singh and Pratibha Vyas, Nanocomposites of Ferrites with TiO2, SiO2 and Carbon Quantum Dots as Photocatalysts for Degradation of Organic Pollutants and Microbes *Magnetochemistry* **2023**, *9*(5), 127; https://doi.org/10.3390/magnetochemistry9050127
12. Bala Anegbe, Ikhazuagbe H. Ifijen, Muniratu Maliki, Ita E. Uwidia & Aireguamen I. Aigbodion Graphene oxide synthesis and applications in emerging contaminant removal: a comprehensive review Environmental Sciences Europe (2024) 36:15 https://doi.org/10.1186/s12302-023-00814-4
13. Naveen Chandra Joshi [a], Prateek Gururani Current Research in Green and Sustainable Chemistry Volume 5, 2022, 100306 https://doi.org/10.1016/j.crgsc.2022.100306
14. Somasekhar Ryali and Paul Douglas Sanasi., Graphene oxide–nano-titania composites for efficient photocatalytic degradation of indigo carmine, Journal of the Chinese Chemical Society 65, 1423 (2018), https://doi.org/10.1002/jccs.201800154.
15. Sunitha Medidi, Sowmyasree Markapurapu, Mastan Rao Kotupalli, Rama Krishna Reddy Chinnam, Venkata Mahalakshmi Susarla, Hima Bindu Gandham, Paul Douglas Sanasi Visible Light Photocatalytic Degradation of Methylene Blue and Malachite Green Dyes with $CuWO_4$-GO Nano Composite Modern Research in Catalysis 7(2),2018 http://doi.org/10.4236/mrc.2018.72002